Article

Assessment of S values in stylized and voxel-based rat models for positron-emitting radionuclides

XIE, Tianwu, ZAIDI, Habib

Abstract

Positron emission tomography (PET) is a powerful tool in small animal research, enabling noninvasive quantitative imaging of biochemical processes in living subjects. However, the dosimetric characteristics of small animal PET imaging are usually overlooked, although the radiation dose may be significant. The variations of anatomical characteristics between the various computational models may result in differences in the dosimetric outcome.

MOLECULAR IMAGING AND BIOLOGY

Mol Imaging Biol (2013) 15:542–551
DOI: 10.1007/s11307-013-0632-0

Published Online: 5 April 2013

World Molecular Imaging Society

RESEARCH ARTICLE

Assessment of *S* Values in Stylized and Voxel-Based Rat Models for Positron-Emitting Radionuclides

Tianwu Xie,[1] Habib Zaidi[1,2,3]

[1]*Division of Nuclear Medicine and Molecular Imaging, Geneva University Hospital, CH-1211 Geneva 4, Switzerland*
[2]*Geneva Neuroscience Center, Geneva University, CH-1205 Geneva, Switzerland*
[3]*Department of Nuclear Medicine and Molecular Imaging, University of Groningen, University Medical Center Groningen, 9700 Groningen, The Netherlands*

Abstract

Purpose: Positron emission tomography (PET) is a powerful tool in small animal research, enabling noninvasive quantitative imaging of biochemical processes in living subjects. However, the dosimetric characteristics of small animal PET imaging are usually overlooked, although the radiation dose may be significant. The variations of anatomical characteristics between the various computational models may result in differences in the dosimetric outcome.

Methods: We used five different anatomical rat models (two stylized and three voxel based) to compare calculated absorbed fractions and *S* values for eight positron-emitting radionuclides (C-11, N-13, O-15, F-18, Cu-64, Ga-68, Y-86, and I-124) commonly used to label various probes for small animal PET imaging. The MCNPX radiation transport code was used for radiation dose calculations.

Results: For most source/target organ pairs, O-15 and Ga-68 produce the highest self-absorbed *S* values because of the high-energy and high-frequency of positron emissions, while Y-86 produces the highest cross-absorbed *S* values because of the high energy and high frequency of γ-rays emission. Anatomical models produced from different rat strains or modeling techniques exhibit different organ masses, volumes, and thus give rise to different *S* values and absorbed dose. The variations of absorbed fractions between models of the same type are less than those between models with different types. The calculated *S* values depend strongly on organ mass, and as such, different models produce similar *S* values for organs of comparable masses. In most source organs presenting with high cumulated activity, the absorbed dose is less affected by model difference compared with other organs.

Conclusions: The produced *S* values for common positron-emitting radionuclides can be exploited in the assessment of radiation dose to rats from different radiotracers used in small animal PET experiments. This work contributes to a better understanding of the influence of different computational models on small animal dosimetry.

Key words: Dosimetry, Small animals, Rat models, PET, Monte Carlo

Introduction

During the last decade, novel radiotracers have been developed for a variety of research applications, mostly

Electronic supplementary material The online version of this article (doi:10.1007/s11307-013-0632-0) contains supplementary material, which is available to authorized users.

Correspondence to: Habib Zaidi; *e-mail:* habib.zaidi@hcuge.ch

focusing on the use of positron-emitting labeled molecular imaging probes to assess noninvasively biochemical processes in living subjects. This has further promoted the usage of small animal positron emission tomography (PET) instrumentation which enables to bridge the gap between *in vitro* science and *in vivo* preclinical studies [1–4]. Rodent species are commonly used in these multicenter longitudinal studies, where the animals are administered significant levels of radioactivity during successive studies that result in radiation doses that might change gene expression, tumor characteristics and in some cases cause lethality [5–7]. Therefore, the dosimetric characteristics of small animal PET imaging require special attention and need to be accurately estimated in laboratory animal experiments.

Many computational models have been developed in internal and external radiation dosimetry of small animals [8, 9]. Depending on the used geometric features to define the anatomical model for radiation transport calculations, computational models can be divided into three types: stylized model which employ simple equation-based mathematical functions, voxel-based models which use matrices obtained from segmented cryosection or medical (CT or MR) images, and hybrid equation-voxel-based models which combine the two aforementioned modeling approaches. Pioneering work was performed by Hui et al. [10] to develop a stylized mouse model for the evaluation of absorbed dose to organs. Flynn et al. [11] used this model to develop a methodology for handling the heterogeneity of tracer uptake in kidney and tumor. Many other stylized mouse [12–14] and rat [15, 16] models have been reported in literature pertaining to radiation dosimetry in small animal models. Likewise, numerous voxel-based mouse [14, 17–21] and rat [18, 19, 22–25] models have been developed and used for small animal radiation dose estimation studies. For the neuroscience community, Beekman et al. [26] developed a high-resolution 3-D rat brain models for molecular neuroimaging research.

Mohammadi et al. [27] and Zhang et al. [28] respectively, evaluated photon-specific absorbed fractions and organ dose conversion coefficients using the Digimouse model [20]. Boutaleb et al. [8] compared calculated *S* values for I-131 between Digimouse and Bitar et al. [21] mouse models. Wu et al. [23], Zhang et al. [24], and Xie et al. [25] developed three computational rat models of different types based on the same rat cryosection images and used them extensively in internal and external radiation dosimetry calculations. Taschereau et al. [29] used an enhanced MOBY model complemented with a high-resolution bladder, femur head and vertebra models for internal dosimetry calculations in small animal PET studies. Larsson et al. [30, 31] studied the absorbed dose to various mouse organs/tissues and inserted tumors using a modified MOBY phantom. In an elegant study, Keenan et al. [9] reported detailed and thorough internal radiation dosimetry calculations using a series of realistic small animal models. More recently, Xie et al. [32] constructed a rat model having detailed and more realistic liver structures to evaluate *S* values and dose distributions for Y-90, I-131, Ho-166, and Re-188 in liver lobes.

In summary, a wide variety of rat models have been developed and used in radiation dose calculations. Evidently, the variations of anatomical characteristics between the various animal models might result in differences between dosimetric estimates. As such, an investigation of the variability in dosimetry calculations across different individual anatomies and model types is commended given its relevance for understanding the uncertainty in the reported dosimetric estimates.

This work focuses on internal radiation dosimetry of rats using common positron-emitting radionuclides. We used five different anatomical rat models (two stylized and three voxel based) to compare calculated absorbed fractions and *S* values for eight positron-emitting radionuclides (C-11, N-13, O-15, F-18, Cu-64, Ga-68, Y-86, and I-124) commonly used to label various probes for small animal PET imaging [33].

Materials and Methods

Computational Rat Models

Table 1 summarizes current computational rat models reported in the literature and their main characteristics. Among the listed models, we selected five different rat models: the models developed by Konijnenberg et al. (Tyco-Rat) [15], Xie et al. (HUST-SRat) [25], Peixoto et al. (UFP-Rat) [22], Wu et al. (HUST-VRat1) [23], and Segars et al. (ROBY) [18]. ROBY is the first NURBS based and is the most popular and widely used rat model. Tyco-Rat is the first stylized rat model whereas the UFP-Rat is the sole voxel-based total-body Wistar rat model. HUST-VRat1 and HUST-SRat are models based on the same dataset of a rat specimen. Figure 1 shows the 3D dorsal views of the five rat models. To minimize the differences between models, the different bones (e.g., skull, ribs, and femurs) and bone marrows were integrated as skeleton. The skeleton was treated as a mixture of 70 % bone, 25 % red bone marrow, and 5 % yellow bone marrow, according to the reported mass proportions of these sub-organs in the rat [34]. The bladder wall and content, the stomach wall and content, the kidney surface and cortex, and the small and large intestine were integrated, respectively, as the bladder, the stomach, the kidney, and the intestine. This treatment was thought reasonable because of uncertainties related to the exact location of these small structures. Common organs in each model were assigned the same organ ID number. The voxel dimensions of the UFP-Rat and HUST-VRat1 were, respectively, $0.71\times0.71\times1.5$ and $0.2\times0.2\times0.4$ mm^3. The voxel-based rat model was generated from the original NURBS-based ROBY model and saved in voxelized format with $160\times160\times620$ matrix dimension and 0.5 mm cubic voxels. The number of voxels in each organ of the UFP-Rat, HUST-VRat1, and voxelized ROBY model were calculated and multiplied by the voxel volume and tissue density to yield the organ mass. The stylized Tyco-Rat and HUST-SRat models were constructed and visualized in MCNPX and

Table 1. Current computational rat models with their main characteristics

Institution	Developer	Model type	Strains	Name	Features	Images	Reference
Johns Hopkins University, USA	Segars et al.	NURBS-based	Wistar rat	ROBY	Total body	MRI	[18]
Mallinckrodt Medical, Tyco Healthcare, The Netherlands	Konijnenberg et al.	Stylized	Wistar rat	Tyco-Rat[a]	Total body	Anatomic images	[15]
Vanderbilt University, US	Stabin et al.	Voxel based	Sprague–Dawley rat	Vanderbilt-Rat[a]	Total body	CT	[19]
	Keenan et al.	Voxel based	Wistar rat	RADAR-Rat[a]	Total body	MRI	[9]
Universidade Federal de Pernambuco, Brazil	Peixoto et al.	Voxel based	Wistar rat	UFP-Rat[a]	Total body	CT	[22]
Huazhong University of Science and Technology, China	Wu et al.	Voxel based	Sprague–Dawley rat	HUST-VRat1[a]	Total body	Cryosection	[23]
	Zhang et al.	NURBS based	Sprague–Dawley rat	HUST-NRat[a]	Total body	Cryosection	[24]
	Xie et al.	Stylized	Sprague–Dawley rat	HUST-SRat[a]	Total body	Cryosection	[25]
	Xie et al.	Voxel based	Sprague–Dawley rat	HUST-VRat2[a]	Total body	Cryosection	[32]
University Medical Center Utrecht, The Netherlands	Beekman et al.	Voxel based	Wistar rat	UMCU-Rat[a]	Brain Model	Cryosection	[26]

[a]Model name is assigned by the authors

SimpleGeo V4.3 [35], where organ volumes were calculated using the Quasi-Monte Carlo method and multiplied by tissue density to yield the organ mass. Table 2 lists the united ID and the calculated mass for each organ of the investigated models.

Absorbed Dose Calculation

The Medical Internal Radionuclide Dose Committee (MIRD) schema [36] was employed to assess S values for positron-emitting radionuclides and the mean absorbed dose $D(r_T,T_D)$ for radiotracers, which is given by:

$$D(r_T, T_D) = \sum_{r_S} \int_0^{T_D} \tilde{A}(r_S, t) S(r_T \leftarrow r_S) \mathrm{d}t, \qquad (1)$$

where $\tilde{A}(r_S, t)$ is the cumulated (time integrated) activity in the source organ/tissue r_S over dose-integration period T_D:

$$\widetilde{A}(r_S, T_D) = \int_0^{T_D} A(r_S, t) \mathrm{d}t, \qquad (2)$$

$S(r_T \leftarrow r_S)$ is the S value describing the equivalent dose rate in the target organ per unit activity in the source organ:

$$S(r_T \leftarrow r_S) = \frac{1}{M(r_T)} \sum_i E_i Y_i \phi(r_T \leftarrow r_S, E_i), \qquad (3)$$

where E_i is the individual energy of the ith nuclear transition, Y_i is number of ith nuclear transitions per nuclear transformation, $M(r_T)$ is the mass of the target tissue r_T, and

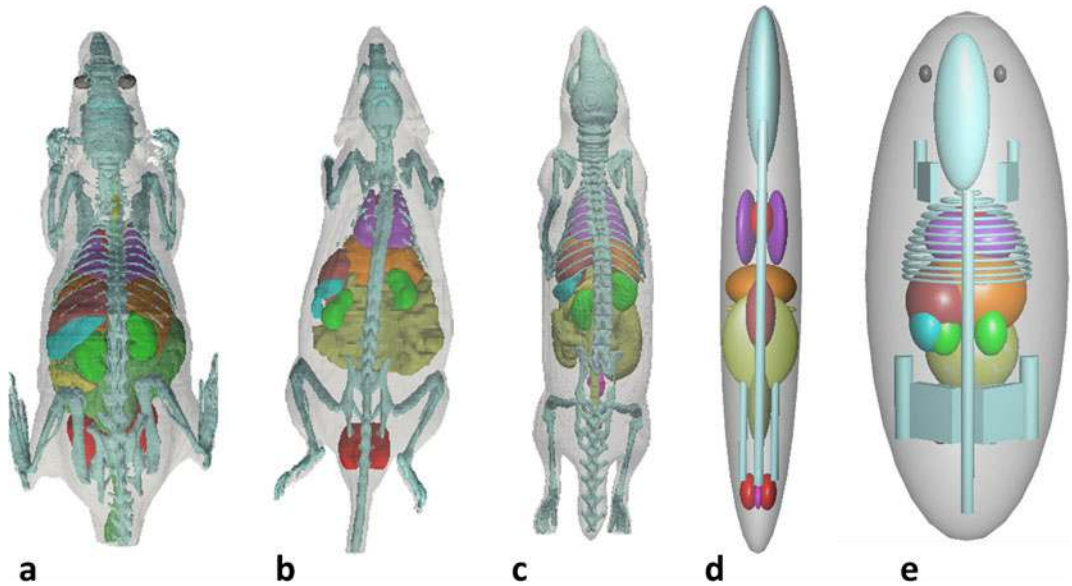

Fig. 1. 3D dorsal views of the various anatomical rat models: **a** HUST-VRat1 [23], **b** UFP-Rat [22], **c** ROBY [18], **d** Tyco-Rat [15], and **e** HUST-SRat [25].

Table 2. Organs masses of the various anatomical rat models (g)

ID	Organ	Organ mass (g)				
		HUST-VRat1 [23]	UFP-Rat [22]	ROBY [18]	Tyco-Rat [15]	HUST-SRat [25]
11	Skeleton	10.67	23.06	33.06	30.59	16.90
12	Heart	1.29	1.66	2.34	1.87	2.23
13	Lungs	0.42	1.09	1.14	3.13	0.82
14	Liver	8.30	11.57	11.13	21.06	9.37
15	Stomach	4.67	2.78	4.84	5.45	4.79
16	Kidneys	1.26	2.10	2.19	3.39	1.50
17	Intestines	14.56	22.94	25.94	23.91	9.44
18	Spleen	0.53	0.58	0.86	0.80	3.24
19	Bladder	0.22	0.16	0.66	0.27	0.29
20	Testes	2.09	2.67	0.17	3.62	2.45
21	Skin	3.60	22.90	19.44	–	–
22	Brain	1.56	–	5.26	7.35	2.11
23	Thyroid	0.02	–	0.27	0.06	0.09
24	Pancreas	1.14	–	0.54	0.86	–
25	Vas def	–	–	0.06	–	–
26	Esophagus	0.07	–	–	–	0.03
27	Eyeball	0.13	–	–	–	0.12
28	Spinal core	0.58	–	–	0.52	–
10	Other tissues	85.29	187.59	235.89	294.67	251.10
–	Total body	136.40	279.09	343.79	397.54	304.49

$\phi(r_T \leftarrow r_S, E_i)$ is the absorbed fraction (AF) which describes the proportion of energy deposited in the target organ and is defined as:

$$\phi(r_T \leftarrow r_S, E_i) = \frac{E_d}{E_i}, \tag{4}$$

where E_d is the energy deposited in the target tissue. When the target organ becomes the source organ, the AF is also termed the self-AF.

Monte Carlo Calculations

The MCNPX general purpose radiation transport code version 2.5 [37] was employed for the calculation of organ absorbed dose for the five rat models. Uniformly distributed photon, positron and electron sources were simulated in 12 chosen source regions. The energy deposited from photons, electrons, and positrons in the target regions were recorded using MCNPX tally card *F8 and used to derive AFs and S values [32, 33]. S values for each particle type emitted were aggregated as the S values for a given radionuclide. A total of 6.0×10^6 primary particle histories were generated such that the statistical uncertainty in terms of coefficient of variation was less than 2 % in most cases. The decay data of the eight positron-emitting radionuclides (C-11, N-13, O-15, F-18, Cu-64, Ga-68, Y-86, and I-124) investigated in this work were obtained from the Health Physics Society electronic resource [38]. The chemical compositions of rat tissues were assumed to be similar to those recommended for humans [39, 40],

Table 3. S values (mGy/MBq·s) for the ROBY model for F-18

Source: F-18

	Skeleton	Heart	Lungs	Liver	Stomach	Kidneys	Intestines	Spleen	Bladder	Testes	Other tissues	Total body
Skeleton	1.14E−03	4.10E−05	9.39E−05	3.14E−05	2.51E−05	2.33E−05	1.56E−05	1.69E−05	2.17E−05	1.95E−05	4.47E−05	1.44E−04
Heart	4.32E−05	1.71E−02	5.39E−04	1.22E−04	5.26E−05	1.91E−05	1.45E−05	2.45E−05	3.97E−06	2.10E−06	3.97E−05	1.55E−04
Lungs	1.00E−04	5.40E−04	2.79E−02	2.05E−04	5.56E−05	2.17E−05	1.42E−05	2.34E−05	4.01E−06	2.54E−06	5.70E−05	1.53E−04
Liver	3.28E−05	1.22E−04	2.04E−04	3.79E−03	1.54E−04	1.10E−04	5.05E−05	4.95E−05	7.62E−06	3.47E−06	3.35E−05	1.57E−04
Stomach	2.65E−05	5.34E−05	5.53E−05	1.54E−04	8.47E−03	7.99E−05	6.14E−05	4.71E−04	9.93E−06	4.41E−06	3.48E−05	1.57E−04
Kidneys	2.38E−05	1.99E−05	2.20E−05	1.12E−04	7.80E−05	1.68E−02	1.14E−04	1.31E−04	2.10E−05	7.43E−06	5.29E−05	1.60E−04
Intestines	1.62E−05	1.39E−05	1.40E−05	5.07E−05	6.13E−05	1.16E−04	1.63E−03	6.75E−05	7.88E−05	1.76E−05	4.00E−05	1.56E−04
Spleen	1.84E−05	2.44E−05	2.40E−05	5.11E−05	4.71E−04	1.31E−04	6.50E−05	4.38E−02	1.26E−05	5.68E−06	4.11E−05	1.54E−04
Bladder	2.31E−05	4.27E−06	3.99E−06	6.56E−06	9.87E−06	2.13E−05	7.83E−05	1.48E−05	5.81E−02	7.75E−05	5.69E−05	1.59E−04
Testes	1.96E−05	2.32E−06	1.70E−06	3.72E−06	4.62E−06	6.60E−06	1.57E−05	6.21E−06	8.13E−05	1.84E−01	6.14E−05	1.37E−04
Other tissues	4.70E−05	3.98E−05	5.63E−05	3.33E−05	3.47E−05	5.22E−05	3.99E−05	4.35E−05	5.78E−05	6.43E−05	1.97E−04	1.46E−04
Total body	1.53E−04	1.62E−04	1.59E−04	1.63E−04	1.64E−04	1.66E−04	1.62E−04	1.62E−04	1.65E−04	1.54E−04	1.54E−04	1.43E−04

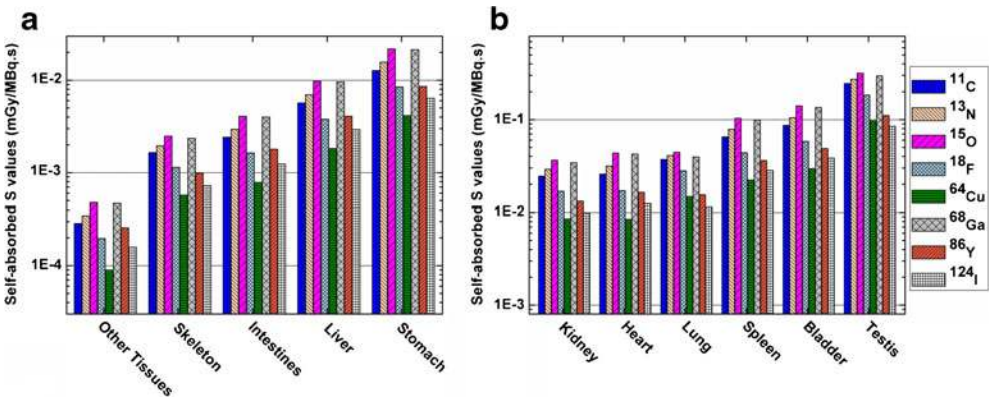

Fig. 2. Self-absorbed *S* values for **a** other tissues, skeleton, intestine, liver, and stomach and **b** kidney, heart, lung, spleen, bladder, and testis of the ROBY model for different positron-emitting radionuclides.

which might introduce additional errors of a few percentage points but these errors are not deemed large enough to affect absorbed dose calculations [9, 32, 41].

Results

Table 3 summarizes calculated *S* values of the ROBY rat model for F-18 in 12 source organs. *S* values for the other positron-emitting radionuclides (C-11, N-13, O-15, Cu-64, Ga-68, Y-86, and I-124) for the ROBY model are given in Tables 1, 2, 3, 4, 5, 6, and 7 in the Electronic Supplementary Material. Figure 2 shows the self-absorbed *S* values for the eight positron-emitting radionuclides for 11 target organs of the ROBY model. For most organs, the largest self-absorbed *S* values are obtained for O-15 and Ga-68 whereas the smallest self-absorbed *S* values are obtained for Cu-64. The self-absorbed organ *S* values for F-18 and Ga-68 are about 55 and 60 % smaller than those obtained for O-15. Figure 3 shows the cross-absorbed *S* values for the eight positron-emitting radionuclides in the ROBY model with the liver being the source region. For most organs, the largest cross-absorbed *S* values are obtained for Y-86. Cu-64 produces the smallest self-absorbed and cross-absorbed *S* values in each source/target organ pair because it emits Auger electrons of low energy (0.8 keV) and high frequency (57 %). Figure 4 illustrates *S* values for the total body irradiating 12 target regions for the eight positron-emitting radionuclides. Except for the skeleton and the testis, the *S* values for all the investigated radionuclides for the total body irradiating other organs are constant and about 10 % higher than self-absorbed *S* values of the total body.

Figure 5 compares the ratios of self-absorbed AFs (Fig. 5a) and cross-absorbed AFs from the stomach (Fig. 5b) in the different rat models to ROBY model for N-13. The AF of ROBY serves as reference because it is widely used in small animal dosimetry studies. For the self-AF of models of the same type, the absolute average difference between the Tyco-Rat and HUST-SRat is 1.4 % whereas it is 7.8 % between the UFP-Rat and HUST-VRat1. In contrast, the absolute average differences of self-AFs between models of different types range between 19.6 and 27.4 %. It was observed that models of the same type provide closer estimated self-AF values. For cross-absorbed AFs, the average difference varies substantially between the models, actually ranging between 33.8 and 392.8 %.

Figure 6 shows self-absorbed *S* values of the heart, the bladder, the skeleton, and the total body in the different rat models for the eight positron-emitting radionuclides. Self-

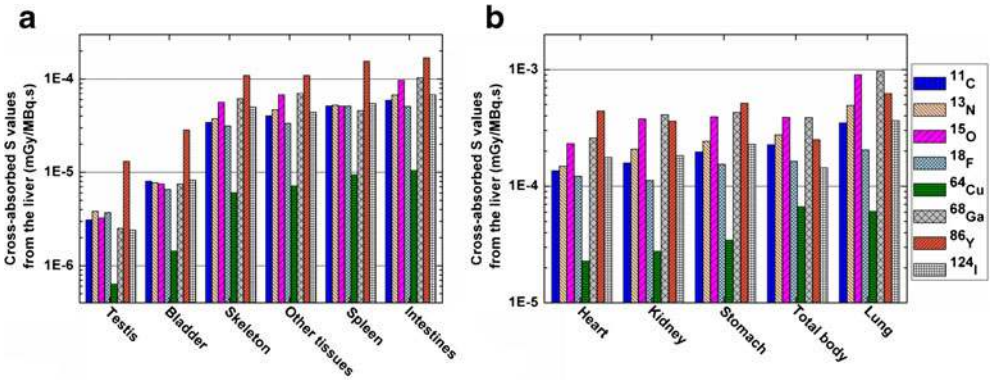

Fig. 3. Cross-absorbed *S* values for **a** testis, bladder, skeleton, other tissues, spleen, and intestines and **b** heart, kidney, stomach, total body, and lung of the ROBY model for different positron-emitting radionuclides with the liver being considered as source organ.

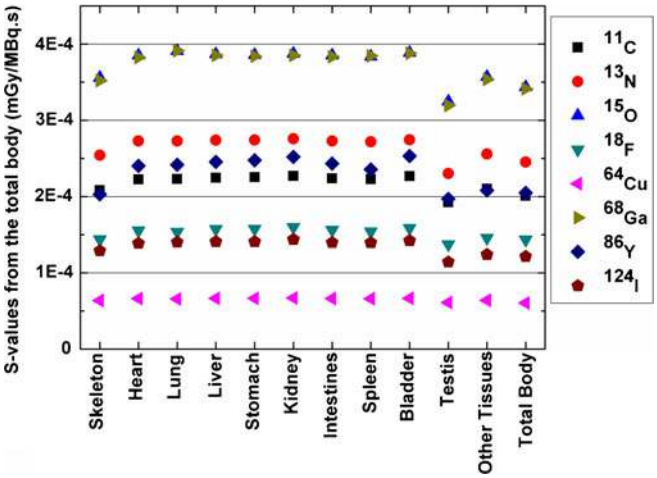

Fig. 4. *S* values for the total body irradiating other regions in the ROBY model for different positron-emitting radionuclides.

absorbed *S* values strongly depend on organ masses in the different models. In the ROBY model, which has the heaviest heart, bladder and skeleton, the lowest self-absorbed *S* value for these organs was obtained for all evaluated radionuclides. The same trend can also be seen in Fig. 6d for self-absorbed total body *S* values for the Tyco-Rat. The Ratios of self-absorbed *S* values of UFP-Rat, HUST-VRat1, Tyco-Rat, and HUST-SRat to the ROBY model for C-11, N-13, O-15, F-18, Cu-64, Ga-68, Y-86, and I-124 are shown in Fig. 7. Organs having a similar mass in the different rat models result in comparable self-absorbed *S* values. Examples of this are the lung and the liver for UFP-Rat and ROBY models, and the stomach for HUST-VRat and ROBY models. Noticeably, the self-absorbed *S* value for the testis is significantly higher in ROBY compared with other rat models because the testis mass is markedly smaller in ROBY, likely owing to individual anatomical deviations between different rat specimens. Figure 8 shows the ratios of cross-absorbed *S* values of the liver irradiating other target organs for different rat models to ROBY. The cross-absorbed *S* values vary markedly between the different rat models and are less correlated with organ mass because they are more affected by source/target distances.

In Table 4, we used published absorbed fraction data of monoenergy photons/electrons by Peixoto et al. [22] and Stabin et al. [19] to calculate the self-absorbed *S* values for F-18 in the heart, kidney, stomach, spleen, and bladder and compared them with those of ROBY and UFP-Rat models used in this work.

We selected from the literature a ^{11}C-labeled probe used in small-animal PET imaging to assess the corresponding absorbed dose to the investigated rat models. ^{11}C-labeled 3-amino-4-(2-dimethylaminomethyl-phenylsulfanyl)-benzonitrilev (^{11}C-DASB) is a recently introduced radiotracer for imaging serotonin transporters using PET [42]. The reported biodistribution data of ^{11}C-DASB were used to calculate the absorbed dose to various organs in the five anatomical rat models. The results are summarized in Table 5 where the compared absorbed dose estimates were limited to common organs usually considered in radiation dosimetry reports.

Discussion

In this work, we used Monte Carlo calculations to compare *S* values of commonly used positron-emitting radionuclides in 5 stylized and voxel-based computational rat models. O-15 and Ga-68 present the largest self-absorbed *S* values in source organs whereas Y-86 produces the largest cross-absorbed *S* values for most source/target organ pairs. Cu-64 presents significantly lower self-absorbed *S* values compared with other radionuclides in most organs. *S* values of organs for positron-emitting radionuclides depend on the source/target distance and the decay scheme of the radionuclide. Radionuclides of high energy and large amount of emitted positrons (e.g., O-15 and Ga-68) are more likely to deliver a very high local dose inside the source organ and the total body. Table 4 compares results from this work with previous published results in the field of small-animal (rat) dosimetry using Monte Carlo simulations and computational models. For the UFP-Rat model, the *S* values reported in this work are slightly lower

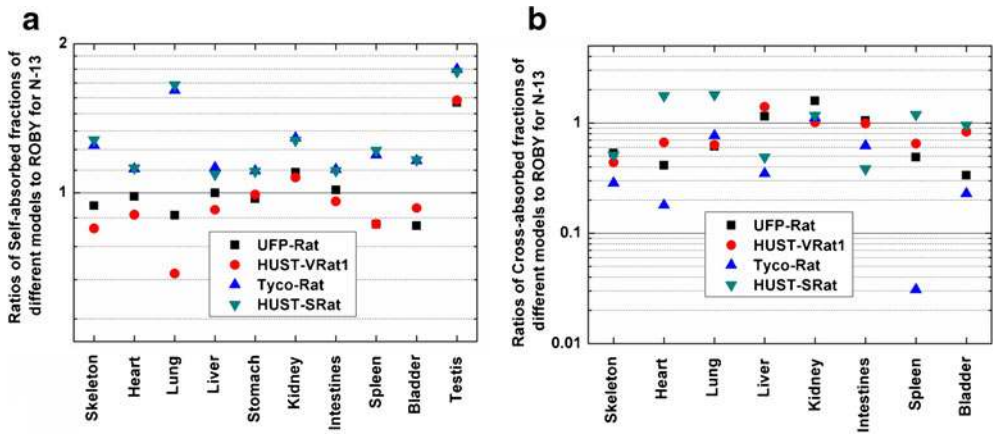

Fig. 5. Ratios of **a** self-absorbed fractions and **b** cross-absorbed fractions from the UFP-Rat (*squares*), HUST-VRat1 (*circles*), Tyco-Rat (*triangles*) and HUST-SRat model (*inverted triangles*) to ROBY of the stomach for N-13.

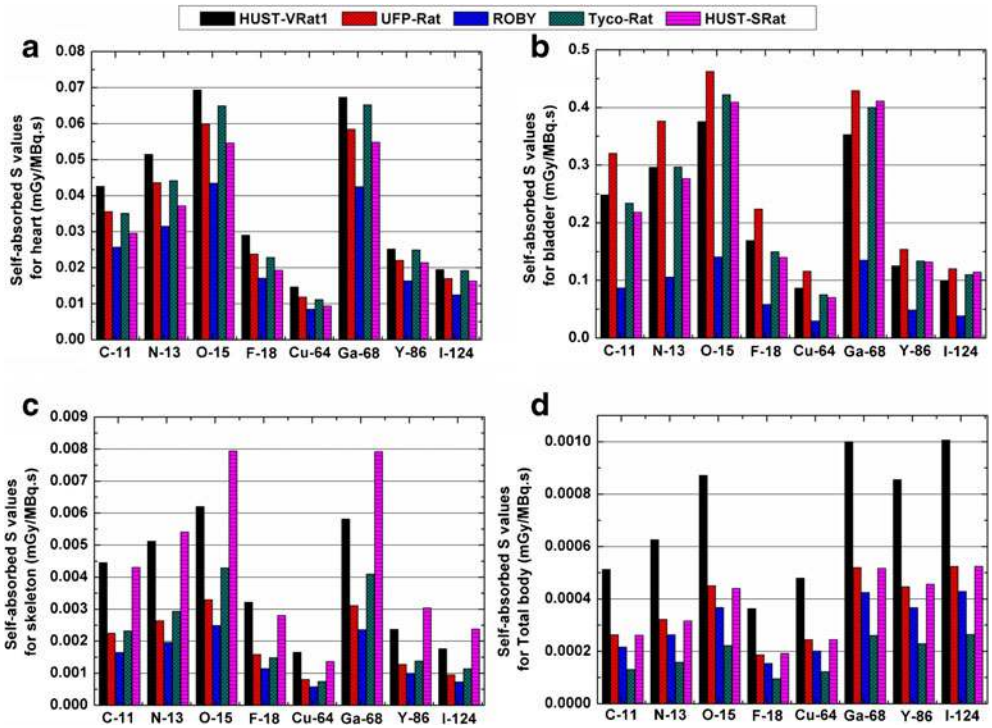

Fig. 6. Comparison of self-absorbed *S* values of **a** the heart, **b** the bladder, **c** the skeleton, and **d** the total body in different rat models for eight positron-emitting radionuclides.

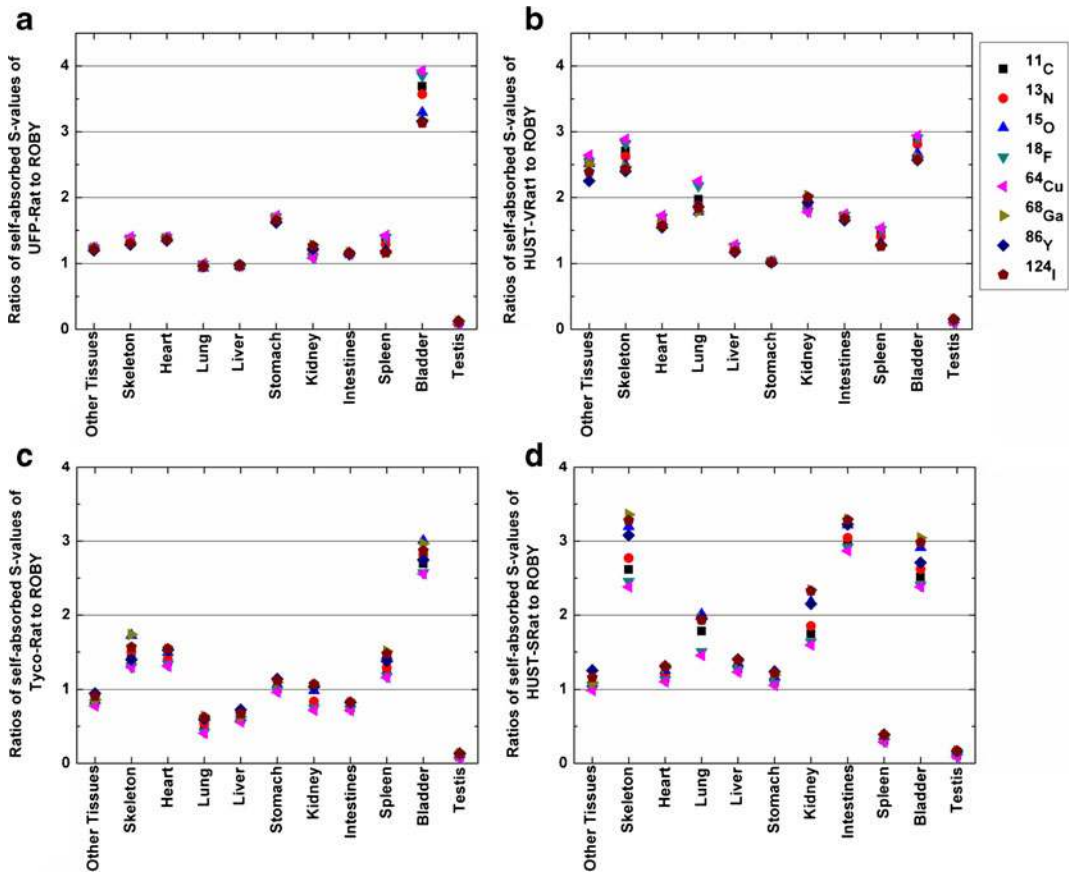

Fig. 7. Ratios of self-absorbed *S* values of **a** UFP-Rat, **b** HUST-VRat1, **c** Tyco-Rat, and **d** HUST-SRat to ROBY model for C-11 (*squares*), N-13 (*circles*), O-15 (*triangles*), F-18 (*inverted triangles*), Cu-64 (*left-pointing triangles*), Ga-68 (*right-pointing triangles*), Y-86 (*diamonds*), and I-124 (*pentagons*).

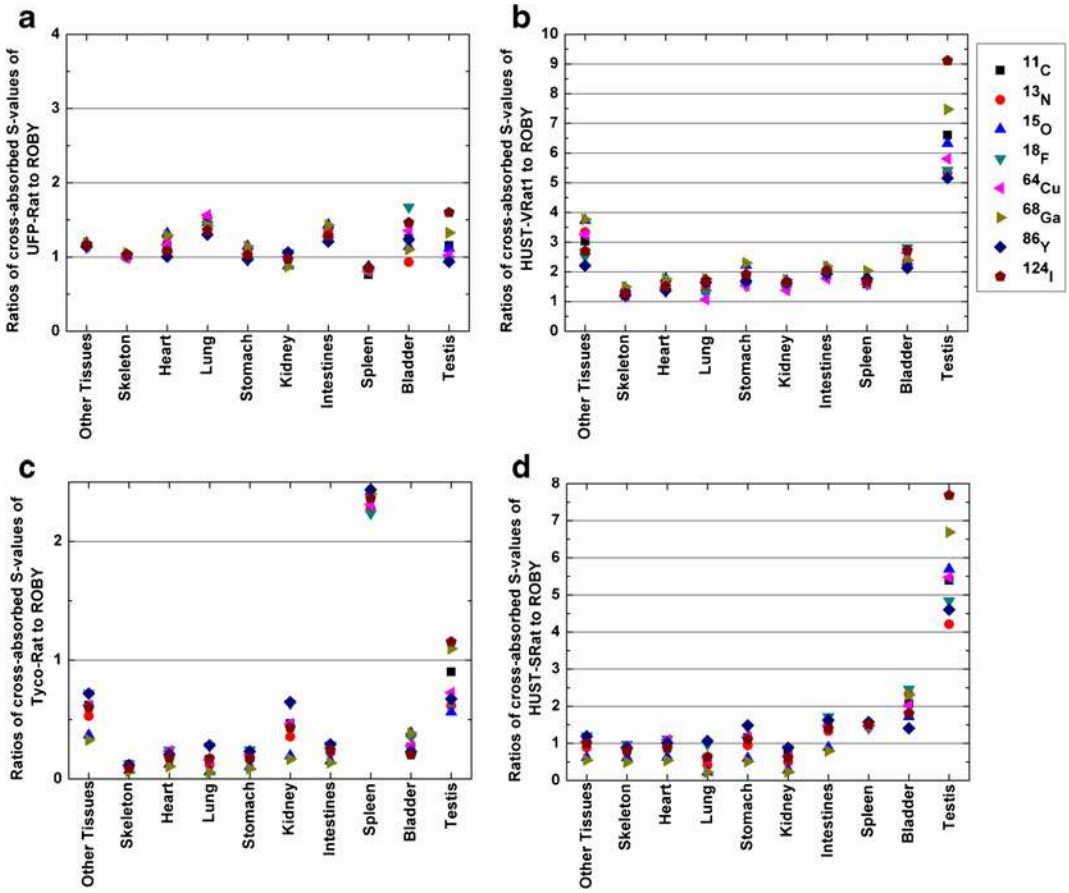

Fig. 8. Ratios of cross-absorbed *S* values from the liver to other target organs of **a** UFP-Rat, **b** HUST-VRat1, **c** Tyco-Rat, and **d** HUST-SRat to ROBY model for C-11 (*squares*), N-13 (*circles*), O-15 (*triangles*), F-18 (*inverted triangles*), Cu-64 (*left-pointing triangles*), Ga-68 (*right-pointing triangles*), Y-86 (*diamonds*), and I-124 (*pentagons*).

(2 % in average) than those calculated from the absorbed fractions of monoenergy photons/electrons. In the Monte Carlo simulation model, we considered the transport of positrons and annihilation photons in a consistent particle history. Few positrons in the source organ may transfer into surrounding tissues and cause electron-positron annihilation outside the source organ, which slightly reduces the amount of energy deposition of secondary particles in the source region. The discrepancies between *S* values among ROBY, UFP-Rat and the results of Stabin et al. can be attributed to individual differences in organ masses and geometries of the different rat specimens.

The impact of using different computational models on dosimetry calculations was also investigated. The self-AFs are similar in models of the same type, a fact that can be explained by the smaller range of secondary electrons and low-energy photons in biological tissues. The higher differences in self-AFs between the voxel-based models suggests that the variation of geometry representation, including differences in terms of organ shape and mass and the dimensions of voxel size, would more severely impact the calculated absorbed fractions in voxel-based models than in stylized models. Considering the case of N-13, the evaluated self-AFs of organs are about 20 % higher in the

Table 4. Comparison of self-absorbed S values (mGy/MBq.s) for F-18 in the heart, kidney, stomach, spleen and bladder of ROBY and UFP-Rat with those of Peixoto et al. [22] and Stabin et al. [19]

Organ	This work		Peixoto et al. [22]	Stabin et al. [19]
	ROBY	UFP-Rat		
Heart	1.71E−02	2.37E−02	2.45E−02[a]	2.70E−02[a]
Kidney	1.68E−02	1.84E−02	1.88E−02[a]	1.76E−02[a]
Stomach	8.47E−03	1.44E−02	1.48E−02[a]	1.62E−02[a]
Spleen	4.38E−02	6.12E−02	6.19E−02[a]	8.69E−02[a]
Bladder	5.81E−02	2.23E−01	2.24E−01[a]	4.21E−02[a]

[a]The *S* values were calculated based on published absorbed fractions of monoenergy photons/electrons by Peixoto et al. [22] and Stabin et al. [19]

stylized model than in the voxel-based model. The AF differences between stylized model and voxel-based model are positively correlated with the energy of emitted particles in the source region.

The rat strain, geometric representation, and information used to produce the various computational rat models used in this work are not equivalent. For instance, the UFP-Rat, ROBY, and Tyco-Rat models were derived from CT slices, MR images, and anatomic measurements of Wistar rats, respectively. Conversely, the HUST-VRat1 and the HUST-SRat were obtained from cryosection images of a Sprague–Dawley rat. Moreover, the UFP-Rat and ROBY models were obtained from images of living animals (MRI or CT images), whereas the Tyco-Rat, HUST-VRat1, and HUST-SRat models were obtained by dissection or cryosection of dead animals. Differences between original animal strains, anatomical data collection methods, and organ identification methodologies all contribute to the observed variations in organ shape, size, location, and mass in the different rat models. Consequently, organ *S* values obtained from various rat models are very disparate, even for models (e.g., UFP-Rat and ROBY) with the same strain (Wistar rat) and geometric representation used for dosimetric calculations (voxel matrix). Unlike the AFs, *S* values do not present obvious consistency between models of the same type or rat strain (e.g., Wistar for UFP-Rat, Tyco-Rat, and ROBY and Sprague–Dawley for HUST-VRat1 and HUST-SRat). This indicates that the rat strain plays a minor role in small animal radiation dosimetry. Since the *S* values strongly depend on organ mass, self-absorbed *S* values in the same organ of similar mass in different models are very close. Therefore, in small animal studies making use of different radionuclides, the use of a reference rat model of similar weight and organ mass to perform the dosimetric assessment is probably wise.

Based on the calculated *S* values and biodistribution data gathered from small animal PET studies, we compared the absorbed dose from ^{11}C-DASB between the various computational rat models. For organs with high radioactivity concentration and normal anatomical features, such as the heart, liver, spleen, stomach, and kidney, the relative standard deviation of absorbed dose estimates between the different models varies from 5.2 to 6.0 %. For organs with high radioactivity concentration and special anatomical features (e.g., narrow geometry, low density, or low mass) which facilitates the escape of particles, such as the skeleton, lung, and testis, the relative standard deviation of absorbed dose estimates between different models varies from 12.7 to 18.1 %. For organs with low radioactivity concentration, such as the bladder and intestines, in which most absorbed dose originates from cross-irradiation, the relative standard deviations of absorbed dose estimates in the different models are all higher than 51 %. The above analysis suggests that for most organs presenting with high activity concentration of radiotracers, the evaluated absorbed dose is less impacted by the different models and would therefore be more equivalent between different rat specimens. The *S* values reported in this work can also be used to evaluate absorbed doses to rats in experimental small-animal PET studies using the MIRD formalism.

Conclusions

We reported *S* values for various rat models from eight positron-emitting radionuclides used in small animal PET imaging and evaluated the impact of variations in rat models on dosimetric estimates. The comparison between the five computational rat models demonstrates that organ size, shape, position, and mass vary considerably between the different models, thus leading to variations in dosimetric estimates. The assessment of AFs of the eight radionuclides reveals that the variations between models of the same type are smaller than those between models of different types. Since *S* values strongly depend on organ mass, the impact of the computational model on *S* values for organs of similar mass is small. For certain radiotracers, the absorbed dose to most organs presenting with high activity concentration is less impacted by the model because the cumulated activity partly compensates the *S* value-induced discrepancy of absorbed dose for these organs. The calculated *S* values for various radionuclides can be used in the assessment of radiation dose to rats from different radiotracers in small animal PET experiments. This work contributes to a better

Table 5. Comparison of ^{11}C-DASB absorbed dose (in mGy/MBq) calculated in the five rat models

Organ	Absorbed dose (mGy/MBq)				
	HUST-VRat1	UFP-Rat	ROBY	Tyco-Rat	HUST-SRat
Skeleton	0.34	0.25	0.23	0.21	0.29
Heart	0.50	0.45	0.42	0.46	0.44
Lungs	1.85	1.85	1.94	2.57	2.80
Liver	1.08	1.08	1.07	1.22	1.16
Stomach	0.48	0.43	0.43	0.44	0.50
Kidneys	1.78	1.74	1.63	1.92	1.89
Intestines	0.73	0.36	0.29	0.13	0.34
Spleen	0.78	0.69	0.73	0.80	0.80
Bladder	0.73	0.34	0.28	0.17	0.31
Testes	0.37	0.29	0.25	0.31	0.29
Other tissues	0.68	0.33	0.27	0.20	0.34

understanding of the influence of different computational models on small animal dosimetry.

Acknowledgments. This work was supported by the Swiss National Science Foundation under grant SNSF 31003A-125246, Geneva Cancer League, and the Indo-Swiss Joint Research Programme ISJRP 138866.

Conflict of Interest. We certify that there is no conflict of interest with any financial organization regarding the material discussed in the manuscript.

References

1. Nanni C, Rubello D, Khan S, Al-Nahhas A, Fanti S (2007) Role of small animal PET in stimulating the development of new radiopharmaceuticals in oncology. Nucl Med Commun 28:427–429
2. Chatziioannou AF (2002) Molecular imaging of small animals with dedicated PET tomographs. Eur J Nucl Med Mol Imaging 29:98–114
3. Aboagye EO (2005) Positron emission tomography imaging of small animals in anticancer drug development. Mol Imaging Biol 7:53–58
4. Levin CS, Zaidi H (2007) Current trends in preclinical PET system design. PET Clinics 2:125–160
5. Russell LB (1971) Definition of functional units in a small chromosomal segment of the mouse and its use in interpreting the nature of radiation-induced mutations. Mutat Res 11:107–123
6. Funk T, Sun M, Hasegawa BH (2004) Radiation dose estimate in small animal SPECT and PET. Med Phys 31:2680–2686
7. Mather SJ (2006) Design of radiolabelled ligands for the imaging and treatment of cancer. Mol Biosyst 3:30–35
8. Boutaleb S, Pouget JP, Hindorf C et al (2009) Impact of mouse model on preclinical dosimetry in targeted radionuclide therapy. Proc IEEE 97:2076–2085
9. Keenan MA, Stabin MG, Segars WP, Fernald MJ (2010) RADAR realistic animal model series for dose assessment. J Nucl Med 51:471–476
10. Hui TE, Fisher DR, Kuhn JA et al (1994) A mouse model for calculating cross-organ beta doses from yttrium-90-labeled immunoconjugates. Cancer 73:951–957
11. Flynn AA, Green AJ, Pedley RB, Boxer GM, Boden R, Begent RH (2001) A mouse model for calculating the absorbed beta-particle dose from (131)I- and (90)Y-labeled immunoconjugates, including a method for dealing with heterogeneity in kidney and tumor. Radiat Res 156:28–35
12. Yoriyaz H, Stabin M (1997) Electron and photon transport in a model of a 30 g mouse. J Nucl Med 38:967–967
13. Hindorf C, Ljungberg M, Strand SE (2004) Evaluation of parameters influencing *S* values in mouse dosimetry. J Nucl Med 45:1960–1965
14. Bitar A, Lisbona A, Bardies M (2007) *S*-factor calculations for mouse models using Monte-Carlo simulations. Q J Nucl Med Mol Imaging 51:343–351
15. Konijnenberg MW, Bijster M, Krenning EP, De Jong M (2004) A stylized computational model of the rat for organ dosimetry in support of preclinical evaluations of peptide receptor radionuclide therapy with (90)Y, (111)In, or (177)Lu. J Nucl Med 45:1260–1269
16. Miller WH, Hartmann-Siantar C, Fisher D et al (2005) Evaluation of beta-absorbed fractions in a mouse model for 90Y, 188Re, 166Ho, 149Pm, 64Cu, and 177Lu radionuclides. Cancer Biother Radiopharm 20:436–449
17. Kolbert KS, Watson T, Matei C, Xu S, Koutcher JA, Sgouros G (2003) Murine S factors for liver, spleen, and kidney. J Nucl Med 44:784–791
18. Segars WP, Tsui BMW, Frey EC, Johnson GA, Berr SS (2004) Development of a 4-D digital mouse phantom for molecular imaging research. Mol Imaging Biol 6:149–159
19. Stabin MG, Peterson TE, Holburn GE, Emmons MA (2006) Voxel-based mouse and rat models for internal dose calculations. J Nucl Med 47:655–659
20. Dogdas B, Stout D, Chatziioannou AF, Leahy RM (2007) Digimouse: a 3D whole body mouse atlas from CT and cryosection data. Phys Med Biol 52:577–587
21. Bitar A, Lisbona A, Thedrez P et al (2007) A voxel-based mouse for internal dose calculations using Monte Carlo simulations (MCNP). Phys Med Biol 52:1013–1025
22. Peixoto PH, Vieira JW, Yoriyaz H, Lima FR (2008) Photon and electron absorbed fractions calculated from a new tomographic rat model. Phys Med Biol 53:5343–5355
23. Wu L, Zhang G, Luo Q, Liu Q (2008) An image-based rat model for Monte Carlo organ dose calculations. Med Phys 35:3759–3764
24. Zhang G, Xie T, Bosmans H, Liu Q (2009) Development of a rat computational phantom using boundary representation method for Monte Carlo simulation in radiological imaging. Proc IEEE 97:2006–2014
25. Xie T, Zhang G, Li Y, Liu Q (2010) Comparison of absorbed fractions of electrons and photons using three kinds of computational phantoms of rat. Appl Phys Lett 97:33702–33704
26. Beekman FJ, Vastenhouw B, van der Wilt G et al (2009) 3-D rat brain phantom for high-resolution molecular imaging. Proc IEEE 97:1997–2005
27. Mohammadi A, Kinase S (2011) Monte Carlo simulations of photon specific absorbed fractions in a mouse voxel phantom. Prog Nucl Sci Technol 1:126–129
28. Zhang X, Xie X, Cheng J et al (2012) Organ dose conversion coefficients based on a voxel mouse model and MCNP code for external photon irradiation. Radiat Prot Dosimetry 148:9–19
29. Taschereau R, Chatziioannou AF (2007) Monte Carlo simulations of absorbed dose in a mouse phantom from 18-fluorine compounds. Med Phys 34:1026–1036
30. Larsson E, Strand SE, Ljungberg M, Jonsson BA (2007) Mouse S-factors based on Monte Carlo simulations in the anatomical realistic moby phantom for internal dosimetry. Cancer Biother Radiopharm 22:438–442
31. Larsson E, Ljungberg M, Strand SE, Jonsson BA (2011) Monte Carlo calculations of absorbed doses in tumours using a modified MOBY mouse phantom for pre-clinical dosimetry studies. Acta Oncologica 50:973–980
32. Xie T, Liu Q, Zaidi H (2012) Evaluation of *S*-values and dose distributions for (90)Y, (131)I, (166)Ho, and (188)Re in seven lobes of the rat liver. Med Phys 39:1462–1472
33. Xie T, Zaidi H (2013) Monte Carlo-based evaluation of *S*-values in mouse models for positron-emitting radionuclides. Phys Med Biol 58:169–182
34. Xie T, Han D, Liu Y, Sun W, Liu Q (2010) Skeletal dosimetry in a voxel-based rat phantom for internal exposures to photons and electrons. Med Phys 37:2167–2178
35. Theis C, Buchegger KH, Brugger M, Forkel-Wirth D, Roesler S, Vincke H (2006) Interactive three-dimensional visualization and creation of geometries for Monte Carlo calculations. Nucl Instrum Meth A 562:827–829
36. Bolch WE, Eckerman KF, Sgouros G, Thomas SR (2009) MIRD pamphlet No. 21: a generalized schema for radiopharmaceutical dosimetry–standardization of nomenclature. J Nucl Med 50:477–484
37. Waters LS, McKinney GW, Durkee JW et al (2007) The MCNPX Monte Carlo radiation transport code. Hadronic Shower Simulation Workshop 896:81–90254
38. HPS (2012) http://hps.org/publicinformation/radardecaydata.cfm
39. ICRP Publication 89 (2002) Basic anatomical and physiological data for use in radiological protection: reference values. A report of age- and gender-related differences in the anatomical and physiological characteristics of reference individuals. Ann ICRP 32:5–265
40. ICRU Report 44 (1989) Tissue substitutes in radiation dosimetry and measurement. International Commission on Radiological Units and Measurements, Bethesda
41. Stabin MG (2008) Uncertainties in internal dose calculations for radiopharmaceuticals. J Nucl Med 49:853–860
42. Wilson AA, Ginovart N, Hussey D, Meyer J, Houle S (2002) *In vitro* and *in vivo* characterisation of [11C]-DASB: a probe for *in vivo* measurements of the serotonin transporter by positron emission tomography. Nucl Med Biol 29:509